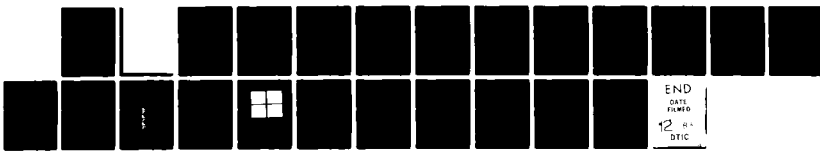


AD-A134 761 ANALYSIS OF STABILITY AND SYMMETRY IMPLICATIONS FOR ICF 1/8
(U) NAVAL RESEARCH LAB WASHINGTON DC

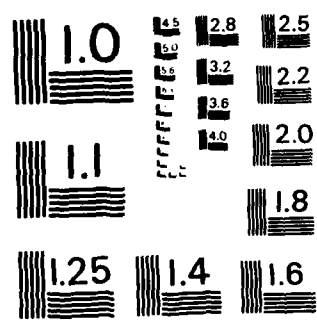
J. H. GARDNER ET AL. 12 OCT 83 NRL-MR-5170

UNCLASSIFIED SBI-AD-E000 550

F/G 17/8 NL



END
DATE
FILED
12-1-84
DTIC



MICROCOPY RESOLUTION TEST CHART
NATIONAL BUREAU OF STANDARDS - 1963 - A

DD FORM 1 JAN 73 1473 EDITION OF 1 NOV 68 IS OBSOLETE
S/N 0102-014-6601

SECURITY CLASSIFICATION OF THIS PAGE (When Data Entered)

SECURITY CLASSIFICATION OF THIS PAGE (When Data Entered)

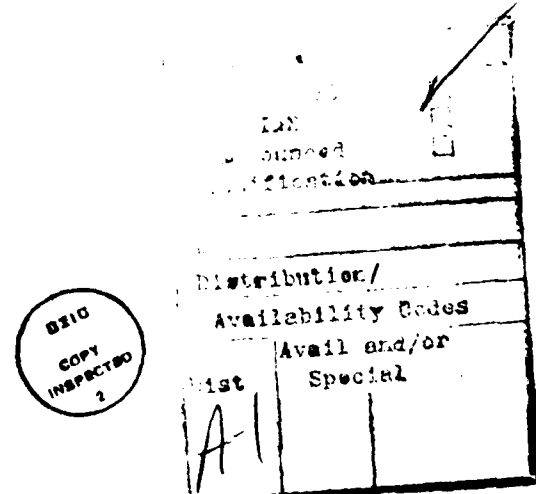
20. ABSTRACT (Continued)

computational work that has been carried out in connection with the experimental work at NRL in evaluating the design constraints that are imposed primarily by the symmetry and stability requirements on directly-driven laser fusion targets.

SECURITY CLASSIFICATION OF THIS PAGE(When Data Entered)

CONTENTS

I. INTRODUCTION	1
II. MODELS USED	2
III. SYMMETRY	4
IV. STABILITY	8
V. SCALING LAWS	13
VI. IMPLICATIONS FOR ICF	17
 REFERENCES	19



ANALYSIS OF STABILITY AND SYMMETRY IMPLICATIONS FOR ICF

I. INTRODUCTION

Pellet gains in excess of 100 will probably be necessary for most applications of inertial fusion.¹ In order to achieve these high gains a number of critical physics elements must be controlled. These include (1) high coupling efficiency, (2) low fuel preheat, (3) implosion symmetry, (4) implosion stability (ablation pressure) and (5) an ignition scheme. These factors interact with each other providing conflicting requirements. In particular the first two items are directly in conflict with the second two. For example, high coupling efficiency and low fuel preheat requires control of deleterious plasma instabilities. These instabilities generally scale as $I\lambda^2$. Therefore they are usually controlled by the use of lower intensities or shorter laser wavelength. But lower laser intensities are generally associated with thinner shell or double shell target designs,² and these higher aspect ratio designs place severe requirements on laser symmetry and target stability. Smoothing out laser nonuniformities by lateral thermal conduction³ requires that the absorption-to-ablation distance be on the order of the target radius, leading to longer, not shorter wavelengths. This separation distance also produces a lower hydrodynamic efficiency. The control of the Rayleigh-Taylor instability by use of smaller aspect ratio targets increases the ablation pressure requirements, and therefore the laser intensity, thus reintroducing the preheat problem. Use of shorter wavelength lasers to reduce the plasma instabilities also reduces the separation distance between the absorption and ablation surfaces thus reducing the effect of thermal smoothing. The problem is then to find a compromise among the competing effects which will lead to an acceptable high gain target. The purpose of this paper is to report on the theoretical and computational work that has been carried out in connection with the experimental work at NRL in evaluating the design constraints that are imposed primarily by the symmetry and stability requirements on directly-driven laser fusion targets.

Manuscript approved June 2, 1983.

We have approached this problem with the viewpoint that sufficiently low intensities will be required that classical physical processes will dominate. Thus we avoid as much as possible the problems of fast electron production and nonclassical energy transport mechanisms. Our philosophy is then to find what limits the critical elements will place on the physically relevant parameters such as target radius, aspect ratio, laser intensity and laser wavelength. We have developed scaling laws that suggest that there is a possible window near 10^{14} W/cm^2 and near 1 μm laser wavelengths.⁴ In deriving our scaling laws we have implicitly assumed that what we desire is a maximum pellet gain Q , and that any laser energy necessary to drive the target can be achieved by building a sufficiently large laser. Laser energy scales as $R^3(\Delta R/R)$ and is strongly dependent on target size but only weakly dependent on irradiance. The constraints that we consider are limits imposed by symmetry, stability, coupling efficiency, preheat, and implosion velocity. We have not yet investigated the constraint imposed by an ignition design as an acceptable design yet eludes us.

Our results are primarily based on numerical simulations with many of the results verified by experiments performed at NRL. Detailed comparisons of code results with experiments are presented elsewhere in this proceedings.⁵ We employ several different types of codes. For the symmetry and stability issues, we use an adaptively gridded, two-dimensional, fully nonlinear, Eulerian computer model (FAST2D) and a triangular grid Lagrangian computer model (SPLISH). Laser matter coupling and scaling laws, relating the asymmetry and stability results to spherical targets, are studied using a one-dimensional, sliding zone, adaptively gridded, fluid code (FAST1D). Principle results to be reported here include: (1) requirements for thermal smoothing of laser nonuniformities. (2) reduced Rayleigh-Taylor growth rates and saturation via the nonlinear Kelvin-Helmholtz shear flow, (3) a new theory based on vortex shedding that explains the reduced linear Rayleigh-Taylor growth rates, and (4) a possible wavelength-intensity window for high gain direct illumination where the requirements of target velocity, symmetry, and now also efficiency can be simultaneously met.

II. MODELS USED

The symmetry and Rayleigh-Taylor stability analysis were performed using the FAST2D laser-shell simulation code. This is a fully two-dimensional nonlinear Eulerian fluid code employing a sliding Cartesian grid with variable grid spacing. The system employs 40 zones transverse to the laser beam and 120 zones parallel to the beam. For the R-T runs we employed a fine grid of

0.25 μm for ten zones on either side of the ablation layer, increasing to a uniform 2 μm spacing for most of the rest of the grid. The code has been run with the fine grid spacing as small as 0.10 μm with no noticeable difference in the results. The refined subzoning moves with the ablation front throughout the course of a run. The zones in the underdense plasma beyond the critical surface and in the low-density rear portion of the foil are exponentially stretched so as to minimize the influence of the boundaries. The code may be run in either planar or cylindrical coordinates with either periodic or outflow boundary conditions in the transverse direction. An option is also available to stretch the outer zones in the transverse direction.

FAST2D solves the time-dependent equations of motion for the continuity of mass, momentum and total energy for a fully ionized ideal gas using the time split, flux-corrected transport algorithms. Thermal conduction is incorporated in a single temperature model using an implicit solution of the two-dimensional classical nonlinear ($\frac{2}{7} K_0 V T^{7/2}$) thermal conduction equation with the standard Braginskii coefficient. Initial conditions are generated from a one-dimensional, analytic, quasi-static equilibrium model.⁶ The analytic model provide a solution which changes only about .5% when FAST2D is tested in one-dimensional nearly-steady-state mode.

Interior layer Rayleigh-Taylor growth is investigated using a Lagrangian fluid dynamics model (SPLISH) which bases its fluid representation on a two-dimensional, dynamically reconnectable grid of triangles. A unique reconnection algorithm allows additional triangles to be added along the shear layer as it stretches in the nonlinear phases of the Rayleigh-Taylor growth and enables the roll up to be followed far into the nonlinear phase where droplets break off and mixing occurs. This model employs ideal nonviscous, nonconducting hydrodynamics appropriate to the high density interior flow.

We investigate the laser plasma coupling and scaling phenomena using our one-dimensional, adaptively gridded, spherical hydrodynamics code (FAST1D). The time-dependent equations for continuity of mass, momentum, and total energy are integrated numerically with sliding zone, Eulerian flux-corrected transport. A flux-conserving scheme is used such that the fluxes between zones results from the difference in fluid and grid velocities. The outer zones and material interfaces move in a Lagrangian manner while intermediary zones move in a prescribed smooth continuous manner so as to maintain the desired resolution near the ablation and critical surfaces. Near the ablation surface the zone size is

held fixed. From the ablation surface to the critical surface the mass per zone is held nearly fixed resulting in increasing zone size. Beyond the critical surface the mass per zone is allowed to increase exponentially. This technique allows a grid resolution of a few tenths of a micron near the ablation surface and a smooth transition to larger zones in the underdense plasma. It has a distinct advantage over Lagrangian codes which find it difficult to enhance the resolution where needed without wasting zones elsewhere.

Thermal conduction is computed using the usual reciprocal average of the classical and limiting heat flux, $l/F = 1/F_{c1} + 1/F_{f1}$ where $F_{f1} = f(kT/m_e)^{1/2} n_e k T V T / |V T|$. This flux limiter F_{f1} is a construct commonly used in fluid codes, for which there is not as yet experimental verification for reactor size plasmas. We have used values of f ranging from 0.6 to 0.03. Our results are mainly quoted for the Bell-Evans-Nicholas⁷ value of $f = 0.1$. The results are insensitive to values of $f > 0.1$ as long as the Mach number at the critical surface is also not too much greater than one (small spherical divergence). Laser light is absorbed by inverse bremsstrahlung of both incoming and reflected light. The fraction of absorbed light not deposited by the inverse bremsstrahlung is deposited smoothly over two zones including the critical surface so as not to generate artificial shocks.

The equations are integrated in strict conservation form. Pressure and temperature are thus derived by subtracting directed kinetic energy from total energy. The fluid equations are closed with an equation of state expressing $P = F(E, \rho)$ and $T = G(E, \rho)$. Near the ablation surface these equations must include the effects of solid material, Fermi-temperature, and fractional ionization. We base our equation of state on the analytic model (ANEOS) in the CHARTD code,⁸ and expansions of the Fermi-Dirac functions by Clayton. This model goes smoothly from a Thomas-Fermi-Dirac model for degenerate electrons at high density and low temperature to a Saha equilibrium at high temperatures and low densities. Such a treatment is necessary in order to correctly calculate the acceleration of near-solid, low-temperature target shells without having the shell compress or explode unrealistically.

III. SYMMETRY

One of the critical elements for high gain target designs is the degree of symmetry that must be maintained in the implosion process. For high gain, the asymmetry of the ablation pressure must be better than a few percent ($\delta P/P < 1-3\%$).¹ Either the laser illumination must be uniform to this percentage, or some additional smoothing mechanism is required. As proposed by Nuckolls,³ lateral thermal conduction could smooth out the laser nonuniformities

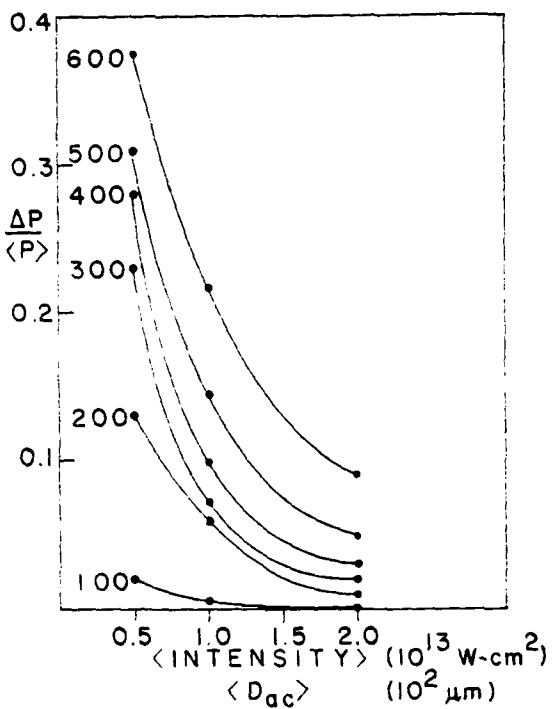


Figure 1. The variation in ablation pressure ($\Delta P / \langle P \rangle$) for all six scale lengths plotted as a function of the average laser intensity ($\langle I \rangle$) and as a function of the average distance from the ablation surface to the critical surface ($\langle D_{ac} \rangle$).

yielding $\delta P / P \ll \delta I / I$ provided the separation of the absorption region and the ablation surface is sufficiently large ($D_{ac} \sim \lambda_s$), where λ_s is the asymmetry wavelength. We have performed a quantitative assessment of this smoothing effect using our two-dimensional laser-shell simulation code FAST2D.

Results are presented for a thin (15 μm thick) plastic (CH) foil accelerated to quasi steady state (6 nanoseconds) by a laser beam with an intensity variation of 40% [$(I_{\max} - I_{\min}) / \langle I \rangle = 0.80$] and a laser wavelength of 1.06 μm . In these simulations the initial conditions were provided by a quasi-static equilibrium model with the relatively-low average laser intensities of $\langle I \rangle = 5 \times 10^{12}$, 1×10^{13} , and $2 \times 10^{13} \text{ W/cm}^2$. The laser beam profile was Gaussian with a reduced intensity in the center of the beam. Since we are only interested in laser asymmetry effects, we invoke the periodicity of the code and only model peak to peak variations. The code was run with the wavelength of the laser inhomogeneity

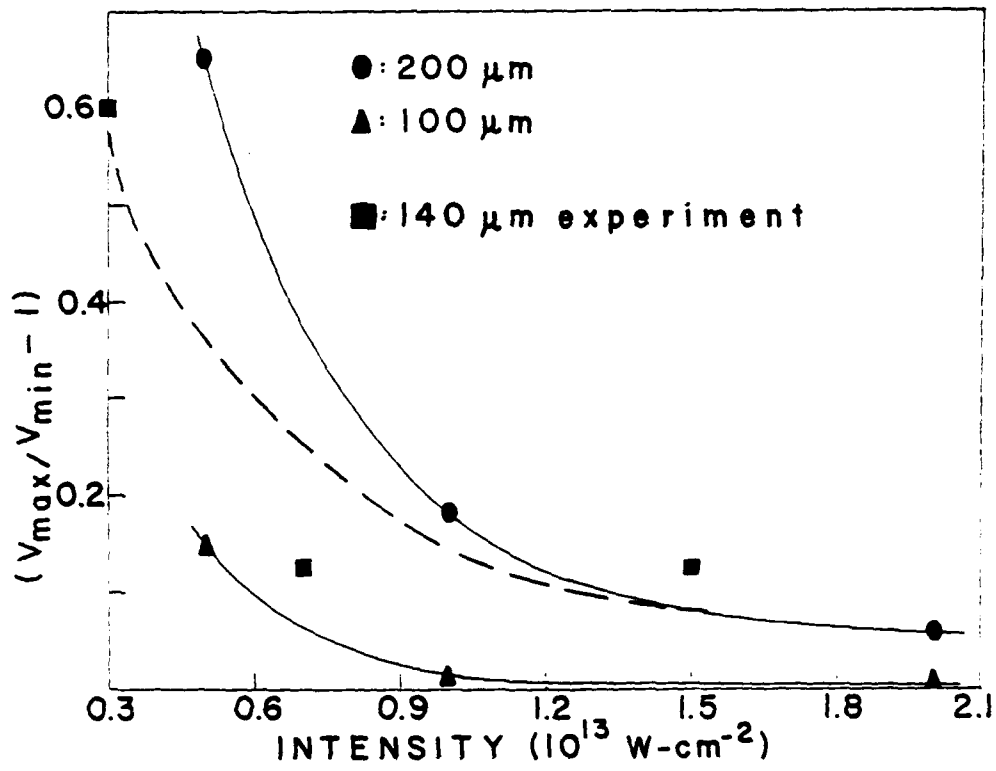


Figure 2. Comparison of the numerical results for the 100- and 200- μm scale lengths with the 140- μm scale length experimental results (Ref. 12) and with the 140- μm theoretical results (dashed curve, Ref. 13).

varying from $\lambda_s = 100$ microns to $\lambda_s = 600$ microns. The results are summarized in Fig. 1, where the variation in ablation pressure is plotted as a function of the average laser intensity, or equivalently the average distance between the ablation and critical surfaces. The direct correlation between D_{ac} and the laser intensity has been noted both experimentally⁹ and theoretically¹⁰.

We find that lateral energy flow in the form of transverse thermal conduction does smooth the effects of laser asymmetries.¹¹ The degree of smoothing is directly related to the distance between the ablation and critical surfaces. The results are in agreement with experimental results obtained at the Naval Research Laboratory¹² and with an analytic model developed at NRL¹³ as shown in Fig. 2 where we compare the foil velocity nonuniformity ($V_{\text{MAX}}/V_{\text{MIN}} - 1$) for the 100 micron and 200 micron asymmetries to experimental results for a 140 micron asymmetry with $I_{\text{MAX}}/I_{\text{MPY}} = 2$. In Fig. 3a-b we present a detailed look at the case where $\langle I \rangle = 1 \times 10^{13} \text{ W/cm}^2$ for $\lambda_s = 100$ microns and 600 microns. Pressure

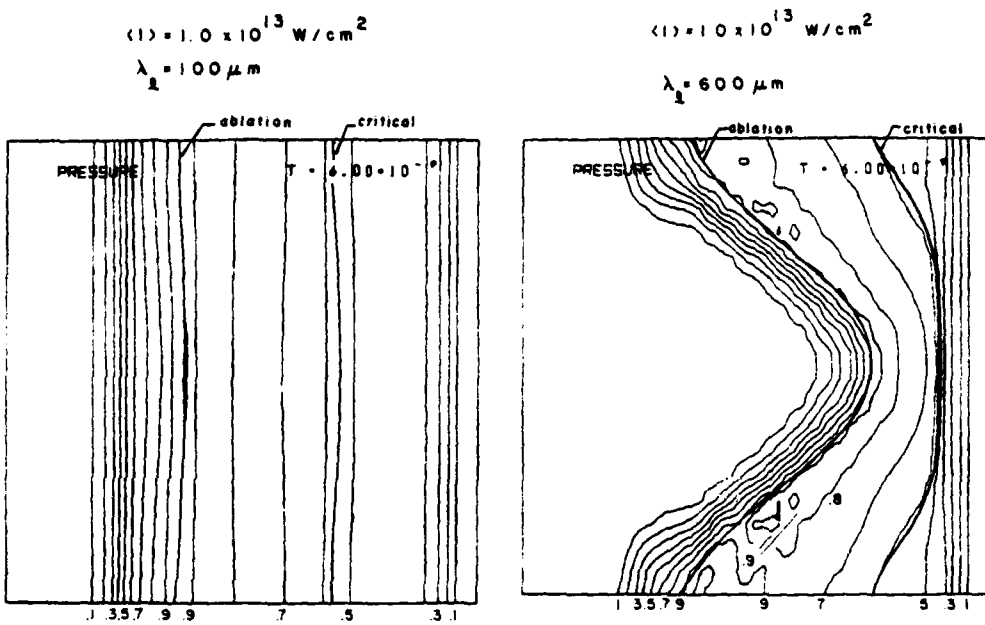


Figure 3. a) Pressure contours for $\langle I \rangle = 1 \times 10^{13} \text{ W/cm}^2$ and $\lambda_s = 600 \mu\text{m}$ increments of 0.5 of maximum pressure. Laser comes in from the right. Note also critical and ablation surface. b) Pressure contours for $\lambda_s = 100 \mu\text{m}$.

contours are in increments of 0.1 counting from the outside inward, and the laser light is coming in from the right. For the 600 micron case severe distortion of the foil has taken place. In the 100 micron case the ablation surface is essentially equivalent to a contour surface and sufficient smoothing has occurred to reduce the ablation pressure variation to 0.5%. This results is basically intuitive. If the scalelengths of the transverse temperature variations are comparable to the separation distance, then a thermal wave propagating transverse to the laser beam should smooth out moderate temperature variations in about the time that the laser energy is conducted to the ablation surface. These simulation results allow us to obtain quantitative estimates of the requirements for thermal smoothing which can be used in scaling arguments.

IV. STABILITY

The stability of the implosion is another critical element for high gain targets. The use of lower laser intensities, and therefore lower ablation pressures, to reduce the plasma instability effects requires the use of higher aspect ratio (thinner shelled) targets. We have investigated the impact that the Rayleigh-Taylor instability has in limiting this aspect ratio.

This instability may grow in the ablation layer or at internal interfaces where materials of different densities abut, whenever the pressure and density gradients have opposite sign. Figure 7 shows four snapshots of a Rayleigh-Taylor unstable interface calculated using our SPLISH model. An initially sinusoidal perturbation becomes nonlinearly distorted into a classical "bubble and spike" pattern as the exponential growth phase begins to saturate. When sufficient shear is generated in the flow by the RT mode, the Kelvin-Helmholtz instability (KH) becomes nonlinearly active and broadens the spike tip, eventually spreading the falling spike material out and rolling it up around the large vorticities which were generated in the density gradient and subsequently advected down the sides of the spikes.

We have modeled the ablation layer Rayleigh-Taylor problem with our two-dimensional laser-shell simulation code FAST2D. Initial conditions are again obtained from the quasi-static equilibrium model. We have modeled the RT instability far into the nonlinear regime beyond the point of foil fragmentation for two types of initial perturbations. One is a multimode perturbation where the first ten modes are excited with equal amplitudes and random phases corresponding to an initial density perturbation of $\pm 4\% [(\rho_{MAX} - \rho_{MIN})/\langle \rho \rangle = 0.08]$.¹⁴ The other is single mode sinusoidal perturbations along the density peak corresponding to a total initial density perturbation of $[(\rho_{MAX} - \rho_{MIN})/\langle \rho \rangle = 0.023]$. The wavelength (λ) is varied in the range $1/2 < \lambda/\Delta R < 10$ where ΔR is the cold foil thickness (20 microns). In both multi-mode and single mode cases we find linear growth rates below classical values by a factor of two to three, and a cutoff in the growth rates for wavelengths less than the cold foil thickness (see Fig. 4).

A striking result we found is the dominance of nonlinear effects in determining the largest viable aspect ratio for thin shell targets. Although the linear growth rates increase as $k^{1/2}$ almost up to the cutoff, the Kelvin-Helmholtz (KH) rollup dominates at large k , reducing the penetration rate of the dense spike below the free fall value and effectively doubling the aspect ratio of the foil.

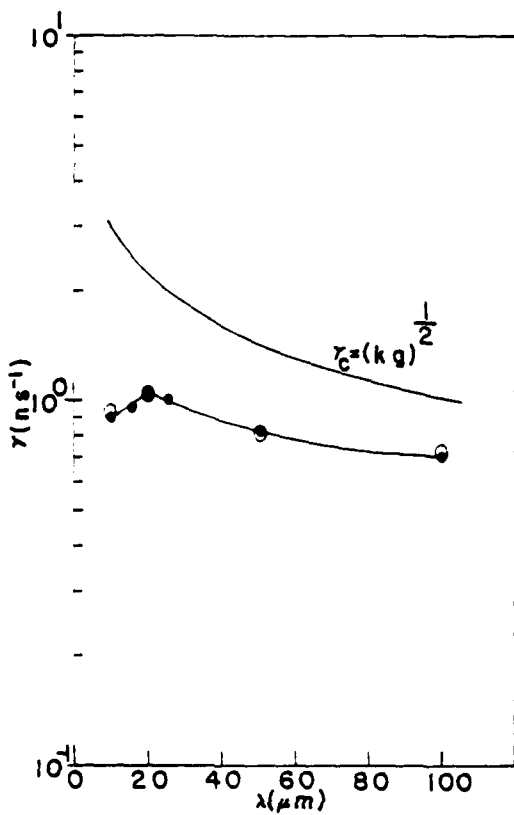


Figure 4. A comparison of the computational growth rates (—●—) to the classical value ($(\text{kg})^{1/2}$, —) and to the vortex shedding theory (○). Cold foil thickness is 20 μm .

The growth rate of the perturbation shifts from exponential to quadratic (free-fall) when the amplitude of the disturbance is on the order of 1/5 the wavelength [$A \sim 0.2 \lambda$]. This results in a different saturation level for the short and long wavelength modes. The amplitude of the large wavelength modes ($\lambda/\Delta R > 1.25$) goes into "free-fall" at a later time and with an effective "free-fall" acceleration comparable to the foil acceleration ($1.5 \times 10^{15} \text{ cm/s}^2$). The exponential growth of the short wavelength modes ($\lambda/\Delta R \leq 1.25$) saturates earlier in time (since the linear growth rates are comparable and the wavelengths shorter) and the "free-fall" acceleration of the spike is reduced by more than a factor of two over the long wavelength modes. This is evident from Fig. 5 where both the "free-fall" acceleration of the spike and the final aspect ratio of the foil are plotted as a function of perturbations wavelength ($\lambda/\Delta R$) for single mode perturbations. This reduced rate of penetration of the dense spike below its "free-fall" value is a direct consequence of the tip-widening brought on by the KH rollup.

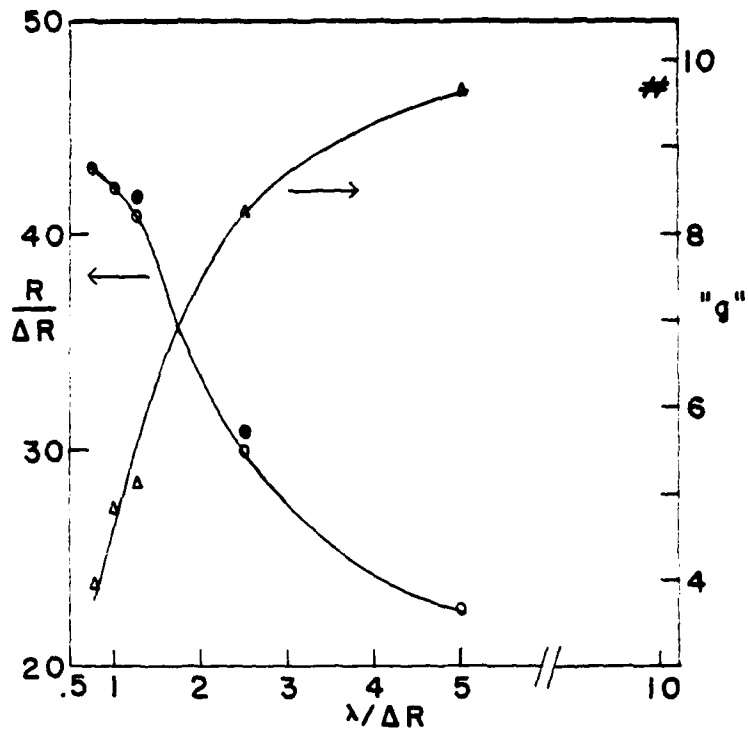


Figure 5. A plot of the "free-fall" acceleration ("g" in units of 10^{14} cm/s^2) of the spike and the final aspect ratio of the foil as a function of the perturbation wavelength ($\lambda/\Delta R$). The solid circles are the aspect ratios obtained with a laser intensity of $5 \times 10^{13} \text{ W/cm}^2$ and the '#' symbol is the aspect ratio obtained with a perturbation wavelength of $200 \mu\text{m}$.

This nonlinear result alters the conclusions one draws with respect to shell integrity as a function of perturbation wavelength. As a result of the earlier saturation of the exponential growth, and the reduced "free-fall" growth, the aspect ratio ($R/\Delta R$) allowable to the short wavelength perturbations has been increased by a factor of two over the long wavelength modes. ΔR is the cold foil thickness ($20 \mu\text{m}$) and R is the distance traveled until the foil uniformity is destroyed. This is defined as the point at which either 35% of the foil mass has been ablated or the rear of the foil was no longer accelerated uniformly. The solid circles are the aspect ratio obtained with a laser intensity of $5.0 \times 10^{13} \text{ W/cm}^2$, where the same effect is evident. The '#' symbol is the aspect ratio obtained for a $200 \mu\text{m}$ perturbation ($I=1.0 \times 10^{13} \text{ W/cm}^2$). As one would intuitively guess, the allowable aspect ratio increases again for perturbation wavelengths very much larger than the foil thickness. Although the linear growth rate increases as $k^{1/2}$ up to the cutoff, nonlinear effects in the form of the KH roll-up are quite effective in saturating the RT instability,

reducing the rate of "fall" of the spike, and increasing the life-time of the foil.

The vorticity, which plays such a dominate role in the non-linear evolution of the RT instability, is also responsible for the reduced linear growth rates. In particular, the shedding of the vorticity generated at the ablation layer is similar to the shedding of vortices that arise from the flow about a bluff body. Not only does this shedding reduce the linear RT growth rate but a symmetric von Karman vortex street develops in the blow off region. The symmetric vortex street is very unstable and thus could also have serious effects on laser absorption, thermal conduction and instabilities in the underdense region.

Figure 6 shows the vortex shedding process from the ablation layer for the 20 μm perturbation wavelength when the system is in the linear regime. The finite-sized vortices are generated by the baroclinic (non-colinear density and pressure gradients) nature of

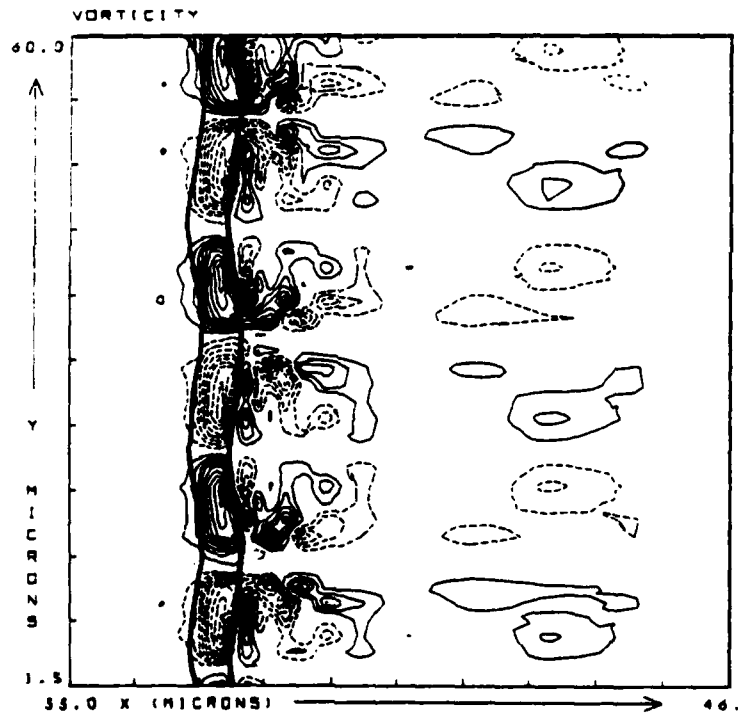


Figure 6. Vorticity contours for the 20 μm mode ($\lambda/\Delta R = 1$) when the system is in the linear regime. The contours are in 10% increments of the maximum vorticity ($+2.75 \times 10^8$, $-2.87 \times 10^8 \text{ s}^{-1}$). The solid (dashed) contours are positive (negative) vorticity. The heavy lines delineate the 10% (right) and 90% (left) density contour.

the profiles. The vorticity generated at the ablation surface is then convected with the flow and shed into the blowoff. This shedding process has a measured Strouhal number (dimensionless shedding frequency) which agrees very well with theory. As a result of this shedding, the classical RT growth rate is reduced. We account for this reduced growth rate by writing $\gamma' = (\text{kg})^{1/2} \cdot \alpha f$, where f is the measured shedding frequency and α is some fraction (less than one). We choose $\alpha = 0.56$ to fit the 20 μm mode. The computational results (—●—) are compared with the classical growth rate ($(\text{kg})^{1/2}$, ——) and the new theoretical results (○). The agreement between the computational results and our vortex shedding theory is excellent (see Fig. 4).

Vorticity continues to be shed from the ablation layer until the spike amplitude becomes comparable to half the perturbation wavelength. At this point the bubble region ceases to ablate and the vorticity is advected down the sides of the spikes where it sets up a reversed flow. It is this secondary flow, the KH rollup, which causes the tips of the spikes to widen and reduces their fall rate. It is apparent that vortex dynamics is playing a dominant role in both the linear and nonlinear phases of the RT instability.

The interior-layer Rayleigh-Taylor problem can occur at many different times and locations during the implosion of a complicated multilayer target. The preignition mix problem is the most familiar situation. This occurs near the final stages of compression of the fuel when the interface between the higher density pusher and the fuel compressionally decelerates. A three-layer mix problem arises where a light fuel layer is separated from a denser pusher shell by a thin but very dense heat-shield layer. Short-wavelength perturbations permit the upper and lower surfaces of the heat shield to move independently, so the RT instability can result even though overall stability is expected at long wavelengths. In order to investigate the nonlinear regime of the RT instability for these two- and three-layer mix problems we have developed a Lagrangian model (SPLASH) which bases its fluid representation on a two-dimensional dynamically reconnectable grid of triangles¹⁵.

In the three layer mix problem the densities of the layers are in the ratio 0.1:2:1 so that the unstable interface has an Atwood number of 1/3. At this Atwood number the evolution of the unstable interface is governed by the interaction between the RT and KH instabilities in both the linear and nonlinear regimes. The evolution of the RT and KH instabilities can be separated into four distinct phases: (1) the initial classical, linear growth phase, ending when the spike-to-bubble height is half the perturbation wavelength, or for thin layers, when the spike to bubble height equals the layer thickness; (2) a saturated RT growth phase with steadily increasing KH rollup and increasing wavelength, ending

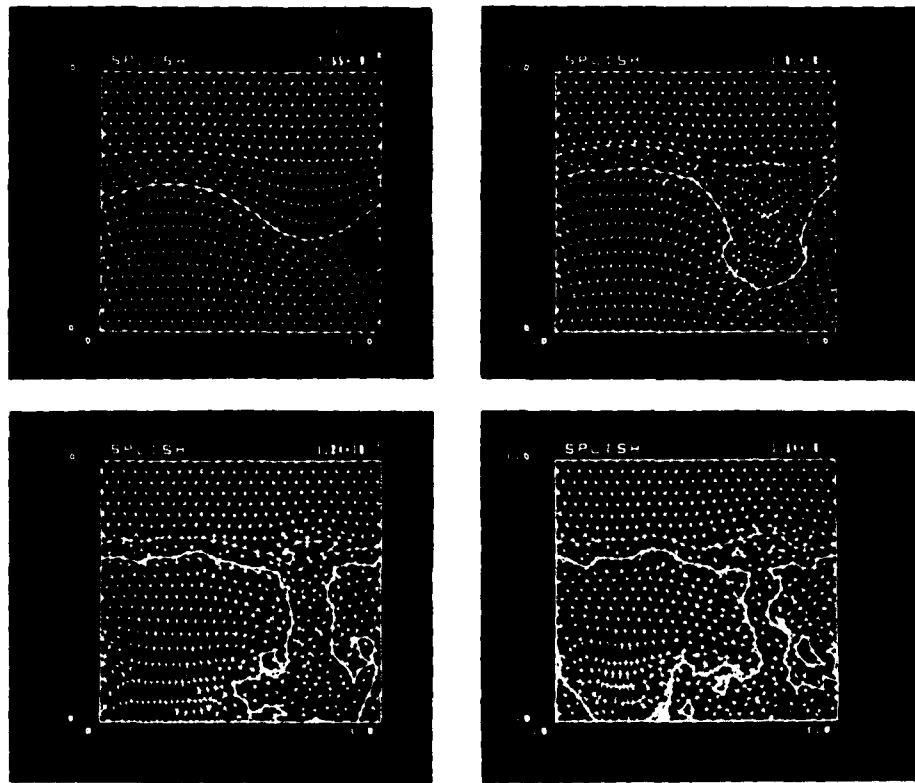


Figure 7. Four stages of the nonlinear evolution of a three layer mix Rayleigh-Taylor instability problem. Density ratios are 0.1:2:1.

when the spike tip becomes wider than the spike body; (3) a small scale structure phase; (4) a turbulent mixing phase (see Fig. 7). The third phase is characterized by downward flow from the thinned layers above the bubbles resembling jets feeding the spike. A stagnation point forms at the point where the jets collide, forcing an upward jet opposed to the spike fall. In the last phase, large amplitude waves run across the stable interface as well, giving rise to jetting and wave-breaking. Many similarities exist between the ablative and nonablative cases. The KH instability plays a major role in both cases in that it reduces the penetration rate of the dense spike below its free-fall value.

V. SCALING LAWS

In order to relate the symmetry and stability results to the design of large reactor size targets, we require scaling laws relating the laser parameters to the target parameters. We have used our one-dimensional spherical hydrodynamics code to determine the scaling laws for (a) separation distance of ablation to critical

surface, and (b) ablation pressure as a function of laser intensity and wavelength.⁴ Rather than attempt to design a set of optimized implosions in these scaling runs we used pure CH shells of constant thickness 125 μm . We used no prepulses to generate artificially large initial separation distances and we ran each case until a quasi-steady state was established. The results are expressed in terms of absorbed irradiance since the absorption process is not well understood for reactor scale plasmas. In our simulations we used pellet radii of 1, 2, and 5 millimeters. Since laser energy scales as $R^3(\Delta R/R)$ a much larger radii would imply either excessive laser energy or aspect ratio. Smaller targets would not contain sufficient fuel for efficient burn and high gain. Even a 1 mm radius pellet is marginally small. Laser wavelengths of 0.53, 1.06 and 2.7 microns in the range of current laser technology were chosen, and intensities were varied from 10^{12} - 10^{15} W/cm^2 . Figure 8 shows a least squares fit to the ablation pressure, as a function of laser intensity and wavelength and target radius of the form $P \sim (I_a \lambda^{-0.25} R^{-0.18})$.⁷ Figure 9 shows D/R as a function of laser intensity for three wavelengths and two radii. This data can be represented by a least squares fit of the form $D/R \sim (I_a \lambda^{3.8})^{0.7}/(R+B)$. In the region of interest $B \approx 1$ millimeter and is only weakly dependent on I_a and λ . This form has the advantage of going to the correct limits for both large and small radii. This surprisingly strong wavelength scaling

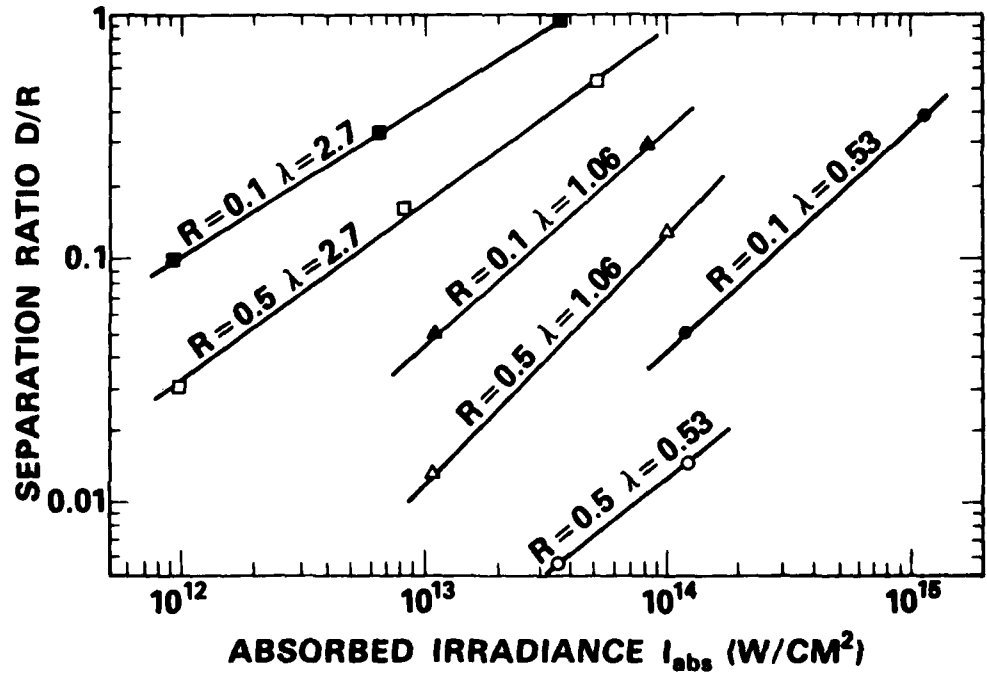


Figure 9. Ablation surface pressure scaling for several laser wavelengths and target radii.

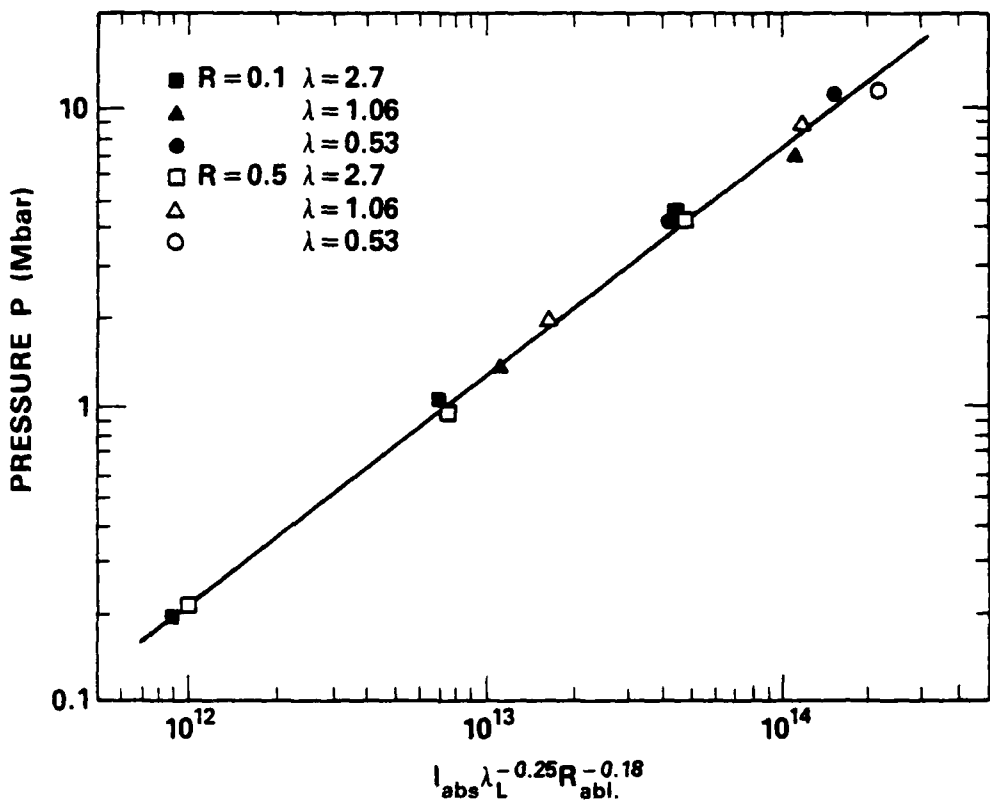


Figure 9. Ratio of distance from ablation to critical surfaces for several laser wavelengths and target radii. A flux limit of $f=0.03$ reduces D/R by roughly a factor of 3-4.

is the result of two factors: longer wavelength light is absorbed at lower densities, and these lower densities have longer scale lengths. Even stronger wavelength scaling has been found in the case of planar ablation.¹³

Use of a strong flux inhibitor only weakly affects the ablation pressure but strongly effects the separation distance from ablation to critical surface. For instance, use of a flux limit $f=0.03$ (commonly quoted) decreases this separation distance by a factor of 3-4.

The hydrodynamic implosion efficiency is another critical element for high gain systems. In performing these simulations we varied the shell thickness and held the final implosion velocity fixed at $V_r = 2.2 \times 10^8$ cm/sec. If most of the kinetic energy can be efficiently converted to compressional energy, then this would be sufficient energy to compress the target to 1000 times solid density at twice the Fermi-degenerate energy. If a relatively unshaped pulse of fixed wave length is used, then the hydrodynamic

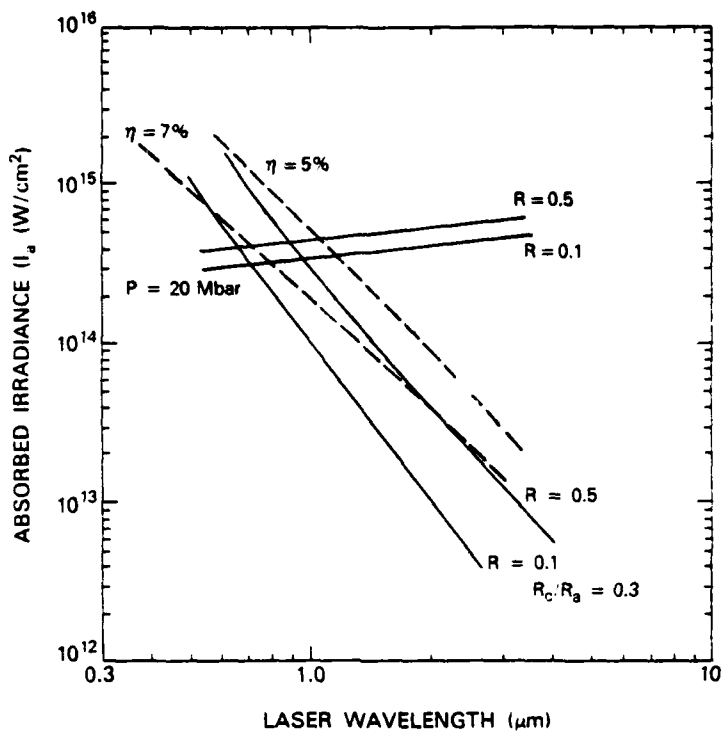


Figure 10. Wavelength-intensity boundaries determined by the symmetry requirements (downward sloping solid curves) and the stability limits (aspect ratio < 20) for two radii pellets (.1 and .5 cm). Constant efficiency of 5 and 7% are shown by dashed line. Operating region is above and to the right of the stability and symmetry boundaries.

efficiency becomes very poor as the target radius approaches collapse. For this reason we choose our aspect ratio such that the final velocity is achieved after the shell has imploded to .4 of its initial radius. The laser driver is then turned off. We then varied the aspect ratio with intensity and wavelength to find the hydrodynamic implosion efficiency given these constraints. The efficiency was found to be relatively insensitive to the target radius for a fixed aspect ratio. However, for fixed separation distance from ablation to critical surface, the efficiency decreased for decreasing laser wavelength! This result is the opposite of what some of our colleagues have predicted. It results because shorter wavelengths require higher laser intensity (given a fixed smoothing requirement). Higher laser intensities produce higher blowoff velocities, and thus lower hydrodynamic efficiency. Figure 10 summarizes the results of the efficiency study by showing contours of equal efficiency superimposed on plots of equal separation ratio and constant ablation pressure.

VI. IMPLICATIONS FOR ICF

High gain targets will require implosion velocity uniformity to better than 1-2 percent.¹ Our flat geometry symmetry results show that if the separation distance D is more than 0.3 times the laser inhomogeneity wavelength, then $\delta P/P < 0.18 I/I$, providing sufficient smoothing for $\pm 10\%$ laser nonuniformities (Fig. 1). We expect roughly the same factor of ten smoothing in spherical geometry if $D/R > 0.3$. Thus one boundary of our design region is given by $D/R = 0.3$ as shown in Fig. 10 for the two limits of target radius.

The stability results indicate that the aspect ratio will be limited to about 20 by the Rayleigh-Taylor instability. This implies an ablation pressure requirement of about 20 Mbars. This result can be obtained from a simple integration of the equations of motion resulting in the relation $P_a \approx 1.5 \langle \rho_0 \rangle v_r^2 (\Delta R_0/R_0)$. Thus another barrier is the requirement that $P_a > 20$ Mbars. The region of acceptable symmetry and stability lies to the right and above these two boundaries.

The requirement of low fuel preheat from plasma instabilities places a limit that scales like $I\lambda^2$. This curve will put a limit to the intensity and wavelength from above. Unfortunately we do not yet possess enough knowledge to predict the absolute location of this a curve on the graph for large scale reactor plasmas and this remains an uncertain parameter.

If we now add results for efficiency, we can see that the highest hydrodynamic efficiency is obtained at the intersection of the smoothing and ablation pressure boundaries. If we go to shorter wavelengths along the symmetry boundary the plasma instability parameter $I\lambda^2$ increases, and the hydrodynamic efficiency goes down. Increasing the wavelength along the fixed pressure boundary curve also increased $I\lambda^2$ and decreases hydrodynamic efficiency. The window for operation, if it exists, should lie between 1/2 micron and 2.7 microns and above 10^{14} W/cm² irradiance. We note that if a pessimistic value of the flux limit, $f=0.03$, is used the smoothing requirement drives the optimum region to 2-3 microns where the efficiency will be even lower.

Several suggestions have been made to overcome the smallness of the $I-\lambda$ window of operation. We have suggested broadband lasers to reduce plasma instabilities,¹ Nuckolls has suggested a series of temporal changes in laser frequency starting at longer wavelengths for smoothing and ending with shorter wavelength for maximum coupling efficiency.¹⁶ McCroy has suggested that the direct laser uniformity may be controlled to better than $\pm 10\%$.¹⁷ Skupsky has suggested that there is enhanced smoothing in the flux-limited regime.¹⁸ One encouraging fact is that absorption by inverse

bremsstrahlung is at lower densities in longer scale length plasmas. If the absorption is at sufficiently low densities, then thermal smoothing beyond the critical surface may take place. For sufficiently large radius pellets we find that the increased inverse bremsstrahlung of shorter wavelength lasers indeed significantly increases the absorption radius. In Fig. 11 we show the location of the critical surface and the 50% absorption surfaces as function of time for red and green laser light for a 5 mm target under similar implosion conditions (shown at the bottom of the figure.) For green light half the energy is absorbed at a distance 3 times the separation distance of the critical to ablation surfaces. This enhanced smoothing may relax somewhat the constraints on thermal smoothing. However we note that the long scale lengths required for this phenomena may also decrease the absorption due to enhanced SBS. Insufficient information is yet available for these long scale length plasmas to draw any definitive conclusions.

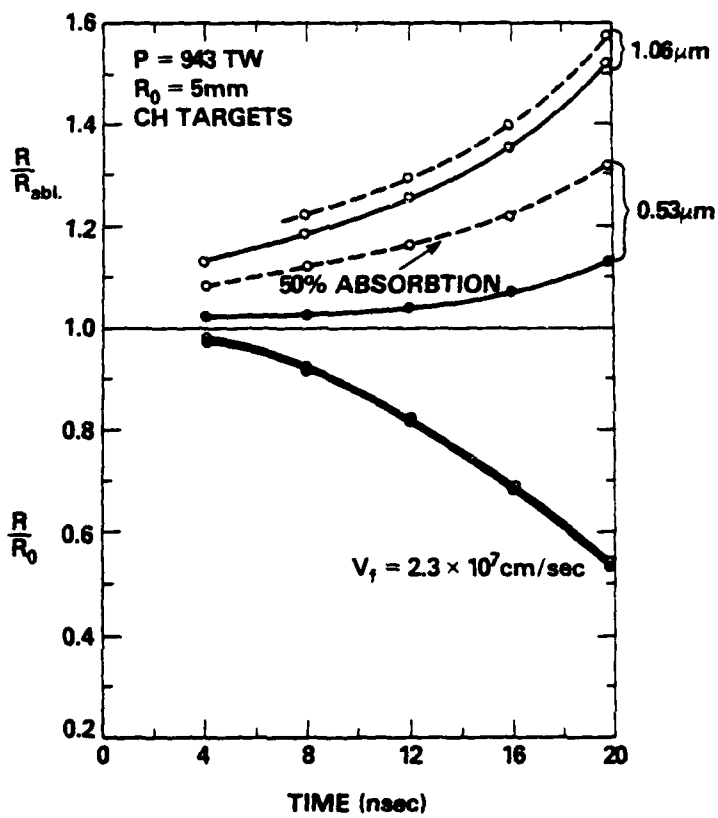


Figure 11. Ratio of separation distance of absorption region from critical surface to target radii as a function of time for red and green light. Lower figure is radius of ablation surface as a function of time. The conditions were picked to match the implosion velocities.

We are still left with a number of uncertainties. First our results are based on hydrodynamic simulations, which neglects possible phenomena such as fast electron transport, filamentation, and other plasma instabilities. As yet no experimental verification exists for the reduced Rayleigh-Taylor results and little is experimentally known about plasma coupling at reactor scale length plasmas. What our results do indicate is that unless an alternative is found to smoothing of laser nonuniformities, short wavelength lasers will have difficulties providing sufficient smoothing for reactor size ICF targets.

We wish to acknowledge many useful discussions with the members of the experimental laser plasma group at NRL. This work was supported by the U.S. Department of Energy and the Office of Naval Research.

REFERENCES

1. S.E. Bodner, Journal of Fusion Energy 1, 221 (1981).
2. Y.V. Afanas'ev et al., ZHETF Pis. Red. 21, 150 (1975) [JETP Lett. 21, 68 (1975)]. J. Lindl, Lawrence Livermore Lab. Report UCLR-30104, 1977 (unpublished).
3. J.H. Nuckolls, L. Wood, A. Thiessen, and G. Zimmerman, Nature (London) 239 193 (1977).
4. J.H. Gardner and S.E. Bodner, Phys. Rev. Lett. 47, 1137 (1981).
5. M.J. Herbst et al. (in this proceedings).
6. J.H. Orens, NRL Memorandum Report 4167, 1980 (unpublished)
7. A.R. Bell, R.G. Evans, and D.J. Nicholas. Phys. Rev. Lett. 46, 243 (1981).
8. S.L. Thompson and H.S. Lauzon, Sandia Laboratory Report SC-RR-710714, 1977 (unpublished).
9. J. Grun, R. Decoste, B.H. Ripin, J. Gardner, Appl. Phys. Lett. 39 545 (1981).
10. J.P. Boris, Comments on Plasma Physics and Controlled Fusion, 3.1 (1977).
11. M.H. Emery, J.H. Orens, J.H. Gardner and J.P. Boris, Phys. Rev. Lett. 48, 253 (1982).
12. S.P. Obenschain et al., Phys. Rev. Lett. 46, 1402 (1981).
13. W.M. Manheimer et al, Physics of Fluids 25, 1644 (1982).
14. M.H. Emery, J.H. Gardner and J.P. Boris, Phys. Rev. Lett. 48, 667 (1982).
15. M.J. Fritts and J.P. Boris, J. Comp. Phys. 31, 173 (1979).
16. J.H. Nuckolls, in Laser Interactions and Related Plasma Phenomena, edited by H. Schwarz and W. Hara (Plenum, New York, 1974) Vol. 3B, p. 416.
17. R.L. McCrory [private communication].
18. S. Skupsky, 12th Annual Anomalous Absorption Conference 10-12 May (1982) Santa Fe, N.M.